CELL BIOLOGY

Cell chirality regulates intercellular junctions and endothelial permeability

Jie Fan[1,2], Poulomi Ray[1,2], Yaowei Lu[3], Gurleen Kaur[4], John J. Schwarz[3], Leo Q. Wan[1,2,4,5]*

Cell chirality is a newly discovered intrinsic property of the cell, reflecting the bias of the cell to polarize in the left-right axis. Despite increasing evidence on its substantial role in the asymmetric development of embryos, little is known about implications of cell chirality in physiology and disease. We demonstrate that cell chirality accounts for the nonmonotonic, dose-response relationship between endothelial permeability and protein kinase C (PKC) activation. The permeability of the endothelial cell layer is tightly controlled in our body, and dysregulation often leads to tissue inflammation and diseases. Our results show that low-level PKC activation is sufficient to reverse cell chirality through phosphatidylinositol 3-kinase/AKT signaling and alters junctional protein organization between cells with opposite chirality, leading to an unexpected substantial change in endothelial permeability. Our findings suggest that cell chirality regulates intercellular junctions in important ways, providing new opportunities for drug delivery across tightly connected semipermeable cellular sheets.

INTRODUCTION

The endothelial cell layer is a semipermeable barrier that tightly controls the passage of proteins and cells in the bloodstream into the interstitial space and regulates the local environment of biological tissues in living organisms (1, 2). Cells achieve this important function largely through mediating paracellular transport by controlling the opening and closing of cell-cell junctions. Despite intense research on vascular signal transduction, current understanding of the role of endothelial morphogenesis in development and disease is still inadequate. In particular, little is known about the role of left-right (LR) polarity, also known as cell chirality, in the regulation of endothelial permeability, which is the focus of our study.

Under normal conditions, endothelial cells are aligned with cobblestone morphology with tightly regulated barrier function provided by intact cell-cell junctions. Disruption of junctional proteins in pathological processes, including inflammatory responses, can increase the permeability of endothelial cells and enhance the paracellular transport of plasma proteins through the opening of gaps between cells (3–5). Elicited by inflammatory factors such as thrombin and tumor necrosis factor, protein kinase C (PKC) enzymes are important mediators of vascular permeability and have been implicated in various vascular diseases including disorders associated with hyperglycemia in diabetes mellitus (6), as well as endothelial injury and tissue damage related to cigarette smoke (7).

The change in endothelial paracellular permeability is often accompanied by the transformation of cell shape, alignment, and junctional morphology (8) and is distinctly associated with cell polarity signaling. The maintenance of a tight endothelial lumen structure requires the proper polarity not only in the direction perpendicular to the lumen surface (i.e., the apicobasal direction) but also within the plane of the endothelial layer. The Wnt/planar cell polarity pathway and its components were found to regulate the organization of the cells within the plane and mediate endothelial cell proliferation, migration, and angiogenesis (9). Cell polarity signaling plays an important role in the regulation of endothelial permeability.

In this study, we focus on the role of the cellular polarity in the LR axis, termed as cell chirality or planar cell shape chirality. Mathematically, cell chirality is handedness (left or right) between three directions: the LR axis, apicobasal axis, and front-rear axis. Since it requires the determination of all these axes at a cellular level, the concept of cell chirality has long been ignored until some recent discoveries, especially with the use of microfabrication technology. This newly discovered cellular property (10–12) has been seen as biased cell alignment (13, 14), directional cell migration (15, 16), asymmetric organelle positioning (17), cytoskeletal dynamic swirling (18), and cytoplasmic torque generation (19). Cell chirality can notably influence the cellular organization in monolayers and account for the overall asymmetry of embryonic development (20), as well as organ-specific asymmetries such as the gut looping (17) and genitalia rotation (21). Now, cell chirality is regarded as an important property of the cell with implications in development and disease. As cell chirality is associated with actin function and actin dynamics (14, 18), we speculated that cell-cell junction and endothelial permeability should be affected by cell chirality because actin filaments play an important role in stabilizing cell junctions.

Previously, we have determined that endothelial cells are strongly right biased, form clockwise-biased monolayers, and undergo directional migration on micropatterned surfaces (14). In this study, we aim to investigate effects of the chiral property of endothelial cells on their function as a physical barrier in blood vessels. Using small-molecule drugs, we observed a PKC activation–dependent, nonmonotonic response of endothelial permeability, accompanied by a simultaneous reversal in cell chirality mediated by the phosphatidylinositol 3-kinase (PI3K)/AKT pathway. Our findings suggest a new mechanism associated with the regulation of endothelial permeability and provide a unique opportunity for controlling local drug delivery across blood vessels.

[1]Department of Biomedical Engineering, Rensselaer Polytechnic Institute, Troy, NY 12180, USA. [2]Center for Biotechnology and Interdisciplinary Studies, Rensselaer Polytechnic Institute, Troy, NY 12180, USA. [3]Department of Molecular and Cellular Physiology, Albany Medical College, Albany, NY 12208, USA. [4]Department of Biological Sciences, Rensselaer Polytechnic Institute, Troy, NY 12180, USA. [5]Center for Modeling, Simulation and Imaging in Medicine, Rensselaer Polytechnic Institute, Troy, NY 12180, USA.
*Corresponding author. Email: wanq@rpi.edu

RESULTS

Endothelial permeability exhibits a nonmonotonic response to PKC activation

We cultured human umbilical vein endothelial cells (hUVECs) on Transwell membranes with a small-molecule PKC activator, (−)-indolactam V

(Indo V; Fig. 1A), and found that the permeability of endothelial monolayers to albumin exhibited a nonmonotonic response at low doses. Indo V and TPA (12-*O*-tetradecanoylphorbol-13-acetate) are widely used membrane-permeable diacylglycerol (DAG) analogs that activate PKC signaling by mimicking DAG, a natural ligand and activator of PKC (*22*, *23*). In the range between 0 and 30 nM of Indo V, endothelial permeability first increased from $4.8 \pm 0.6 \times 10^{-6}$ to $10.5 \pm 0.5 \times 10^{-6}$ cm/s (from 0 to 20 nM) and then decreased to $7.5 \pm 0.4 \times 10^{-6}$ cm/s (at 30 nM) (Fig. 1B). Consistent with the change of endothelial permeability, the TEER also displayed the lowest resistance at 20 nM Indo V (Fig. 1C). It should be noted that at a much higher concentration (100 nM), which is widely used in the literature (*24*, *25*), the permeability increased to ~3-fold of the control at a value of $15.2 \pm 2.7 \times 10^{-6}$ cm/s (fig. S1A), together with a significant decrease of TEER (fig. S1B). While the effects of high-level PKC activation have been studied on endothelial permeability, the variation of permeability at a relatively low level of PKC activation (i.e., the increase of permeability at 20 nM Indo V and the subsequent decrease at 30 nM) has not been documented before. We therefore explored the underlying mechanism.

Junction formation was suppressed under the intermediate-level PKC activation

To investigate the mechanism underlying the permeability change, we studied cell-cell junction formation at different levels of PKC activation. Zonula occludens–1 (ZO-1) at the endothelial junctions plays a crucial role in maintaining the integrity of both tight junction and adherens junction (*26*). Compared to the continuous ZO-1 structure found with the 0 and 30 nM Indo V groups, the cell layer treated with 20 nM Indo V showed a distorted and compromised ZO-1 morphology (Fig. 1D). We quantified the junctional ZO-1 formation by calculating the percentage of the positively stained pixels that had the intensity above the mean cytoplasmic intensity (Fig. 1E). There was a significantly lower ZO-1 assembly at the junctions in the 20 nM Indo V group compared to the 0 and 30 nM groups (Fig. 1F). In addition, the number of intercellular gaps, indicated by white arrowheads in Fig. 1D, increased by three times when Indo V increased from 0 to 20 nM and decreased when Indo V further increased to 30 nM (Fig. 1, G and H). The intercellular gaps are classified as open spaces located between adjacent cells in a confluent monolayer and enclosed by cell boundaries with weakly stained junction proteins while containing no cell nucleus. Higher concentrations of Indo V (100 nM) caused significant junctional disruption (fig. S1, C to E) and a remarkable permeability increase (fig. S1A), which was probably caused by a lower cell density, compared to the control, due to side effects of the high doses of the drug (fig. S1F).

We further investigated the morphology of junctional vascular endothelial (VE)–cadherin (fig. S2, A to G). Although VE-cadherin remained at a similar level on cell borders (fig. S2, F and G), the staining appeared to be diffused in the 20 nM Indo V group (fig. S2A), and the kurtosis value was much lower than those of the control and the 30 nM Indo V group (fig. S2, B to E), indicating less organized VE-cadherin structures at 20 nM Indo V. This was consistent with the poor tight junction formation indicated by ZO-1 staining. These results together suggest that increased permeability at the intermediate-level activation of PKC is associated with the poor formation of cellular junctions.

Poor junction formation is associated with mismatched cellular biases

We confirmed the increase of PKC levels with Indo V treatment at lower concentrations (i.e., 0 to 30 nM) using enzyme-linked immunosorbent assay (ELISA), and a linear relationship was observed (fig. S3A). To further explore the mechanism associated with the poor formation of cellular junctions, we examined the cellular metabolic activity, motility, and overall expression of cadherin proteins (fig. S3, B to J). We found, after 48 hours of higher doses of Indo V treatment, that the overall metabolic activity of endothelial cells in Transwell, measured by the time-coursed colorimetric tetrazolium salt (MTT) assay, was lower than that of the control, probably due to a lower cell density (fig. S1F). In contrast, lower doses of Indo V treatment (0 to 30 nM) did not lead to significant effects on the metabolic activity (fig. S3B) or motility measured from the time-lapsed cell tracking analysis (fig. S3, C to I). Furthermore, we did not find significant changes in N- or VE-cadherin expression within the range of PKC activation (fig. S3J), consistent with previous reports (*27*).

We then studied cell polarity and chirality on the Transwell membrane by staining cell borders with a ZO-1 antibody, centrosomes with a pericentrin-1 antibody, and cell nuclei with DAPI (Fig. 2, A to D). The nucleus-centrosome axis is widely regarded as the front-rear polarity axis (*28–30*), and cell centroid positioning relative to this axis defines the LR polarity or cell chirality (Fig. 2D). We found that, without drug treatment, cell centroids predominately fell on the right side of the nucleus-centrosome axis (Fig. 2E).

To test the relevance of our in vitro model to endothelial physiology, we examined cell chirality in endothelial tissues (fig. S4, A to D). For all the tissues that we examined (human umbilical cord veins, mouse vena cava, mouse thoracic aorta, and mouse aortic arch), the endothelial cells showed a predominately rightward bias (fig. S4, E and F), consistent with the chirality that we observed in vitro. Although these endothelial tissues are exposed to different flow patterns [the vena cava and the thoracic aorta are exposed to laminar flow, while the aortic arch (inner curvature) is exposed to turbulent flow (*31*)], all endothelial cells show a dominant rightward bias (fig. S4G). This is consistent with that observed on two-dimensional (2D) patterns without fluid flow, indicating that cell chirality does not depend on flow conditions and is a relatively stable property of the cell.

In the 2D endothelial cell monolayer, we further found that cell centroids appeared on the left side of the nucleus-centrosome axis at 30 nM Indo V (Fig. 2E), while at 20 nM, the positioning of cell centroids seemed randomized. To investigate whether cellular biases are associated with the disruption of the cellular junction, we classified the endothelial junctions as right-right (R-R), right-left (R-L), and left-left (L-L) according to the biases of adjacent cells (Fig. 2C). There were significantly less ZO-1 assembly and more intercellular gaps at the R-L junctions, compared with the R-R and L-L junctions (Fig. 2, F and G). This finding suggests that cellular biases affect endothelial junction and the regulation of permeability.

Cell chirality is dependent on the level of PKC activation

As the observed LR biases are intrinsically defined and reflect the handedness or chirality of the cells, to confirm the dependence of the cellular biases on PKC activation, we determined cell chirality with a 2D micropatterning method, as described previously (*14*). The cell alignment was first determined from the intensity gradient between the interior region and the contour of the cell in phase-contrast images (*32*). The chirality of the cells was defined by the angle of the cell alignment deviating from the circumferential direction on a ring-shaped micropattern, where the "positive" and "negative" alignment angles stood for the counterclockwise (CCW; leftward) and clockwise (CW; rightward) biases, respectively (fig. S5). The hUVECs exhibited CW alignment with negative
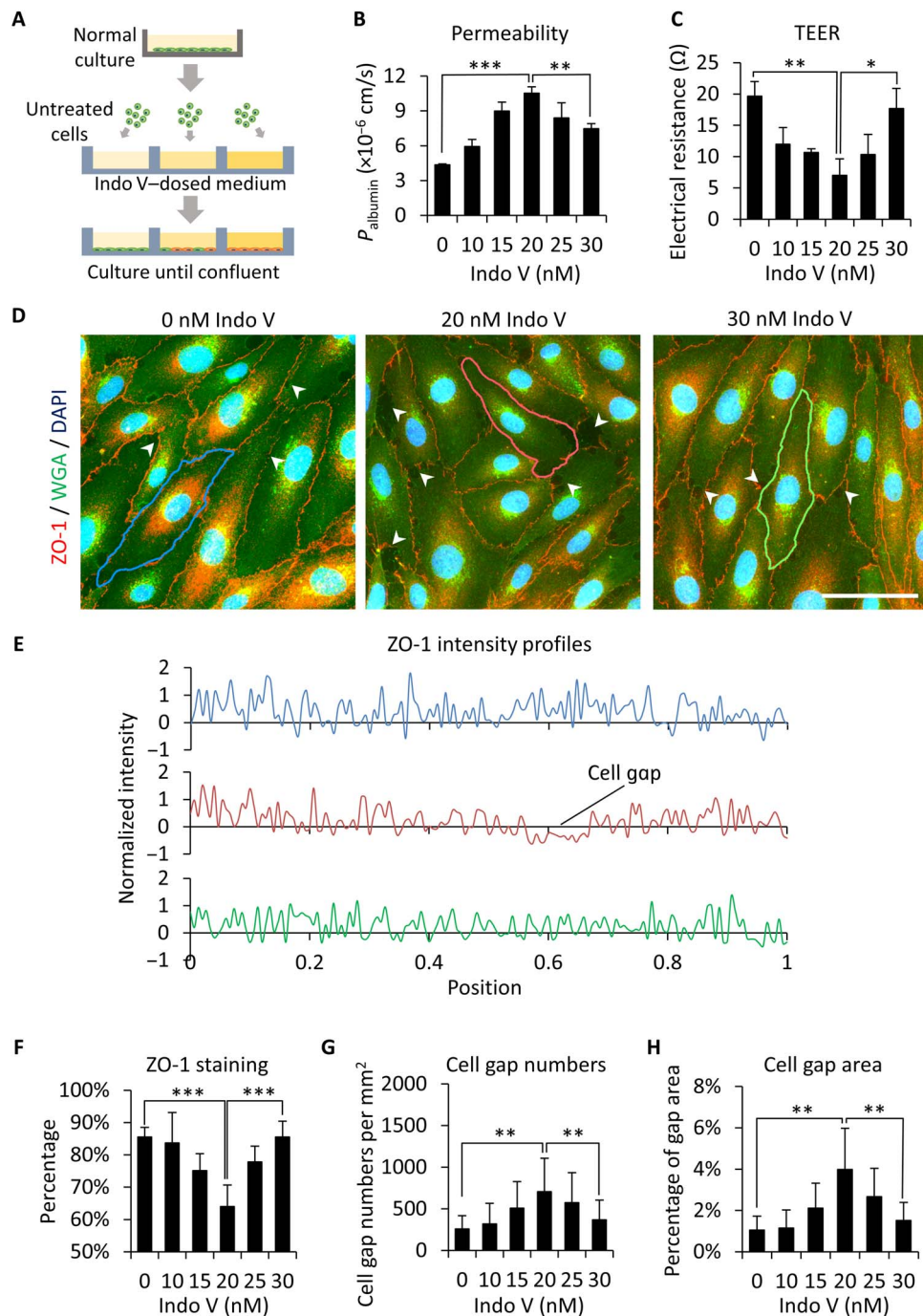
Fig. 1. PKC activation changes endothelial cell permeability. (A) Schematic of Transwell culture of endothelial cell monolayers to determine their dose-dependent responses in permeability and transendothelial electrical resistance (TEER) when the cells were exposed to Indo V, a specific PKC activator. (**B** and **C**) Permeability and TEER of the hUVEC monolayer with Indo V treatment. Data are presented as average ± SD ($n = 3$). *$P < 0.05$; **$P < 0.01$; and ***$P < 0.001$ by one-way analyses of variance (ANOVAs) with the Bonferroni-Holm method between groups. (**D**) Immunofluorescence images of hUVEC monolayers on the Transwell membrane labeled with Alexa Fluor 568 ZO-1 (1A12, red), Alexa Fluor 488 wheat germ agglutinin (WGA), and 4',6-diamidino-2-phenylindole (DAPI) (blue). Significantly fewer junctions and more intercellular gaps (white arrowheads) were formed on the hUVEC monolayer treated with the 20 nM Indo V (scale bar, 50 μm). (**E**) The fluorescence ZO-1 intensity profile along the entire border of a cell [blue, red, and green outlines shown in (D), respectively]. The reported intensity is calculated as the junctional ZO-1 intensity subtracted by the average cytoplasm intensity and then normalized pixel by pixel by the WGA intensity along the cell border. The positive intensity represents junctional ZO-1 formation. (**F**) Percentage of positively stained ZO-1 along the entire cell border as a function of Indo V concentration. Data are presented as average ± SD ($n = 11$ images for the 0 nM group, $n = 12$ images for the 20 to 25 nM groups, $n = 13$ images for the 30 nM group). ***$P < 0.001$ by one-way ANOVAs with the Bonferroni-Holm method between groups. (**G** and **H**) Intercellular gap number and area of Indo V–treated cell monolayers on the Transwell membrane. Data are presented as average ± SD ($n = 11$ images for the 0 nM group, $n = 12$ images for the 10 to 25 nM groups, $n = 13$ images for the 30 nM group). **$P < 0.01$ by one-way ANOVAs with the Bonferroni-Holm method between groups.
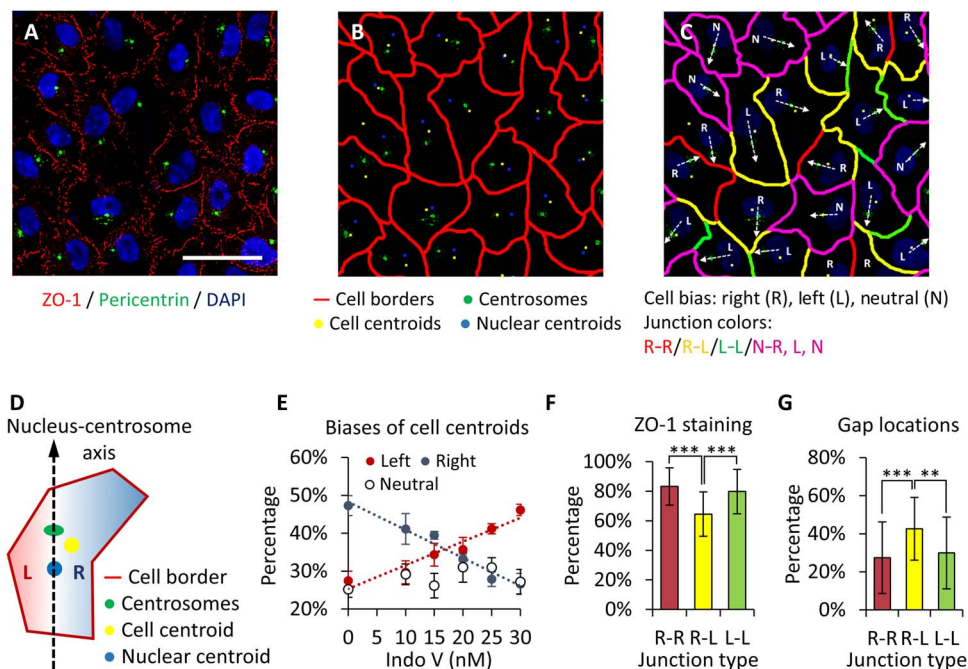
Fig. 2. Cell chirality affects endothelial junction formation. (**A**) Immunofluorescence images showing cell nuclei (DAPI, blue), centrosomes (Alexa Fluor 488 pericentrin, green), and junctions (Alexa Fluor 568 ZO-1, 1A12, red) (scale bar, 50 μm). (**B**) Image segmentation along cell-cell junctions (red), shown with the centroids of nuclei (blue), centrosomes (green), and the centroids of cell bodies (yellow). (**C**) Cell junctions were classified as "R-R", "R-L", and "L-L" on the basis of the LR biases of two adjacent cells. The white arrows represent the nucleus-centrosome axes, while the left or right positioning of cell centroids (yellow) shows the LR biases. (**D**) Schematic of determination of the left (L) or right (R) cell bias based on the biased positioning of the cell centroid relative to the nucleus-centrosome axis in (C). (**E**) LR biases of individual cells in the monolayer with Indo V treatment. Data are presented as average ± SEM (n = 7 images, N = 380 cells for the 0 nM group; n = 6 images, N = 294 cells for the 10 nM group; n = 6 images, N = 288 cells for the 15 nM group; n = 6 images, N = 298 cells for the 20 nM group; n = 6 images, N = 270 cells for the 25 nM group; n = 6 images, N = 276 cells for the 30 nM group). (**F**) Percentage of ZO-1 staining along the R-R, R-L, and L-L junctions. Data are presented as average ± SD (n = 307 for R-R, n = 309 for R-L, n = 537 for L-L). ***$P < 0.001$ by one-way ANOVAs with the Bonferroni-Holm method between groups. (**G**) Normalized percentage of intercellular gap locations at the three types of junctions. Data are presented as average ± SD (n = 37 images for each group). **$P < 0.01$ and ***$P < 0.001$ by one-way ANOVAs with the Bonferroni-Holm method between groups.

alignment angles (Fig. 3A), as reported previously (*14*). The chirality of endothelial cells was altered under the Indo V treatment (Fig. 3A). When treated with 30 nM Indo V or above (up to 1000 nM as shown in fig. S6), the cells switched to a dominant CCW bias, with positive angles of cell alignment in the circular histogram. At an intermediate concentration of 20 nM, the Indo V treatment resulted in a nonbiased distribution of alignment angles. We also statistically examined the number of the rings showing CW, CCW, or nonchiral (NC) alignment and found a dose-dependent reversal of cell chirality (Fig. 3, B and C), with 71% CCW rings at 30 nM Indo V versus 92% CW rings for the control group. A single variable, chiral factor (CF), was introduced and defined by comparing ring numbers from the following formula: CF = (number of CW rings − number of CCW rings)/(number of total rings), with CF = +1 standing for complete CW and CF = −1 for complete CCW. With Indo V concentration varying from 0 to 30 nM, the CF value changes from 0.9 to −0.8. Similarly, we used TPA as an alternative to Indo V to activate PKC signaling in the endothelial cells (fig. S7) and noticed a similar nonmonotonic response, with ~0.3 nM TPA leading to a loss of cell chirality (fig. S7, A to D), increased cell permeability (fig. S7E), and decreased TEER of endothelial cells (fig. S7F). Using time-lapse imaging of micropatterned endothelial cells, we found that PKC activation reversed the directional bias of endothelial cell migration at physical boundaries from rightward to leftward (movies S1 to S4). Combining the data on cell chirality and permeability, we found that

endothelial cells exhibited the highest permeability and lowest TEER when the CF was close to zero (Fig. 3D). By examining ZO-1 staining, we again confirmed poor junction formation between endothelial cells at an intermediate level of PKC activation, suggesting that strong uniform chiral biases promote the formation of cell-cell junctions (Fig. 3E). Altogether, our data suggest that the loss of cell chirality may lead to poor cell alignment and result in the inferior integrity of multicellular monolayer.

Mismatch of cell chirality results in poor endothelial integrity

To further demonstrate the effects of cell chirality on endothelial barrier integrity, we established a coculture model of the CW or right-biased cells (normal cells without treatment) and CCW or left-biased cells (cells pretreated with Indo V for 24 hours) (Fig. 4A). We found that 24-hour pretreatment can lead to a complete reversal of cell chirality for at least 24 hours (fig. S8, A to C). We then measured the chirality, permeability, and TEER of the coculture of the two abovementioned cells at different ratios. We confirmed that the cell number and metabolic activity were similar among all groups (fig. S8, D and E). We found that a 50:50 mixture of CW and CCW cells led to a significantly higher permeability and a lower electrical resistance, compared to both 100% CW cells and 100% CCW cells (Fig. 4, B to F). The permeability again peaked when the CF was close to zero.
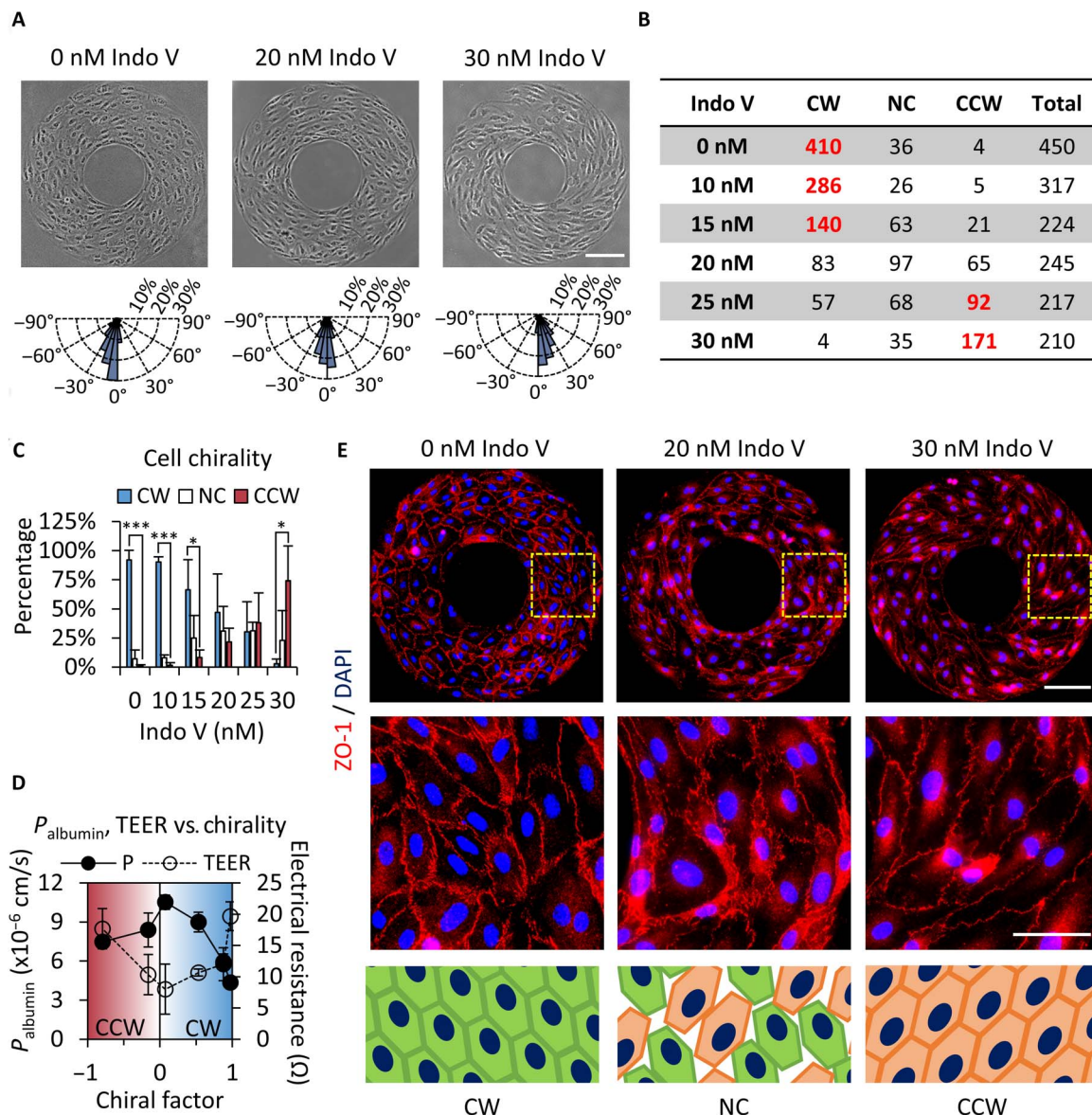
Fig. 3. PKC activation mediates cell chirality. (**A**) Phase-contrast images and cell alignment angles of the micropatterned hUVECs at different doses of Indo V (scale bar, 100 μm). (**B**) Numbers of CW, NC, and CCW rings of hUVECs with Indo V treatment. Bold red font indicates dominant chirality and significant difference at $P < 0.05$ by rank test. (**C**) Percentage of CW, NC, and CCW rings of hUVECs with Indo V treatment. Data are presented as average ± SD ($n = 6$ experiments, $N = 450$ rings for the 0 nM group; $n = 4$ experiments, $N = 317$ rings for the 10 nM group; $n = 3$ experiments, $N = 224$ rings for the 15 nM group; $n = 3$ experiments, $N = 245$ rings for the 20 nM group; $n = 3$ experiments, $N = 217$ rings for the 25 nM group; $n = 3$ experiments, $N = 210$ rings for the 30 nM group) *$P < 0.05$ and ***$P < 0.001$ by Student's t test (unpaired, two tailed). (**D**) Permeability and TEER of hUVEC monolayer versus cell CF, defined as (number of CW rings − number of CCW rings)/number of total rings. The CFs were calculated from the ring numbers in (B). Data are presented as average ± SD ($n = 3$ for permeability and TEER data). (**E**) Top row: Immunofluorescence images of hUVECs on the ring-shaped micropatterns labeled with Alexa Fluor 568 ZO-1 (1A12, red) and DAPI (blue) (scale bar, 100 μm). Middle row: Magnified images of the yellow boxed area (scale bar, 50 μm). Bottom row: Schematics of the CW, NC, and CCW cell alignment on micropatterns.

Furthermore, the coculture of CW and CCW cells also resulted in disordered cell alignment and discontinuous ZO-1 formation, compared to the monoculture (Fig. 4G). This was reflected by the decrease in staining of junction proteins and the increase in intercellular gap number and size (Fig. 4, H to J).

To further understand the junction formation of cells with opposite chirality, we fluorescently labeled the CW cells before mixing with the CCW cells and classified the cell junctions again into three groups, CW-CW, CW-CCW, and CCW-CCW, on the basis of the chirality of two adjacent cells identified by fluorescence (Fig. 4K). It showed less ZO-1 staining and more intercellular gap formation at the CW-CCW junctions, while no significant differences were found between CW-CW and CCW-CCW junctions (Fig. 4, L and M). Altogether, our data suggest that the mismatch of the chirality of adjacent cells can lead to the poor formation of cell-cell junctions.

To examine whether cell chirality is implicated in known mechanisms for the regulation of endothelial permeability, we tested effects of additional chemicals on cell chirality. The inhibition of focal adhesion
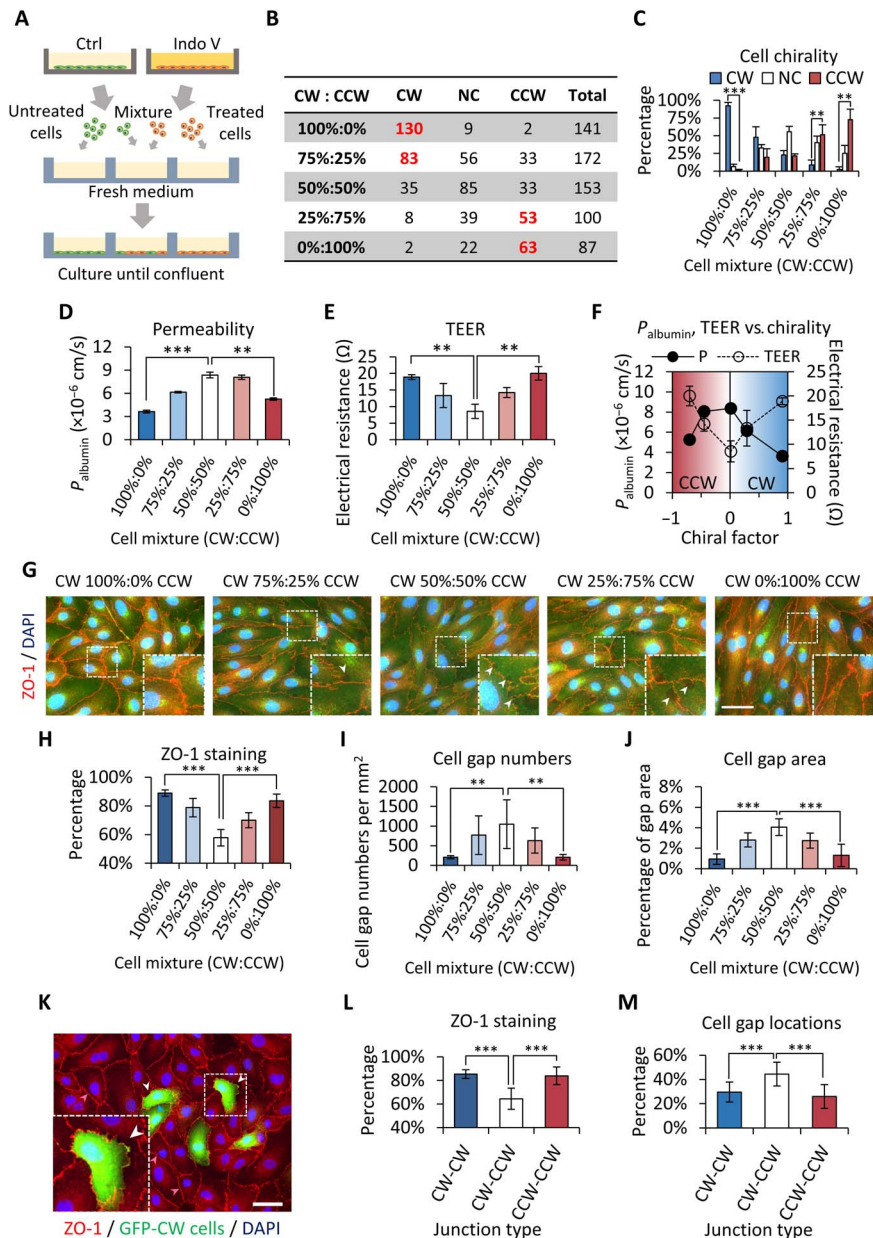
Fig. 4. Mixing CW and CCW cells results in higher permeability and disrupted monolayer integrity. (**A**) Schematic diagram of mixed culture of CW (untreated) and CCW (Indo V treated) hUVECs for permeability and TEER measurement. (**B** and **C**) Variation of the numbers and the percentages of hUVEC ring patterns that shows different chirality as a function of the ratio of cell mixture. Bold red font in (B) indicates dominant chirality and significant difference at $P < 0.05$ by rank test. **$P < 0.01$ and ***$P < 0.001$ by Student's t test (unpaired, two tailed). (**D** and **E**) Permeability and TEER of the hUVEC mixture. Data are presented as average $\pm$ SD ($n = 3$). **$P < 0.01$ and ***$P < 0.001$ by one-way ANOVAs with the Bonferroni-Holm method between groups. (**F**) The permeability and TEER of the hUVEC mixture versus cell CF, calculated from the ring numbers in (B). Data are presented as average $\pm$ SD ($n = 3$ for permeability and TEER data). (**G**) Immunofluorescence images of the hUVEC mixture on the Transwell membrane labeled with Alexa Fluor 568 ZO-1 (1A12, red), Alexa Fluor 488 WGA, and DAPI (blue) (scale bar, 50 μm). Significantly fewer junctions and more intercellular gaps (white arrowheads in magnification windows) were formed on the hUVEC monolayer with a mixing ratio of 50% CW versus 50% CCW. (**H** to **J**) Percentage of positively stained ZO-1 along the entire cell border and variation of intercellular gap number and size on cell mixture. Data are presented as average $\pm$ SD ($n = 11$ for each group). **$P < 0.01$ and ***$P < 0.001$ by one-way ANOVAs with the Bonferroni-Holm method between groups. (**K**) Immunofluorescence image of the hUVEC mixture with green fluorescent protein (GFP)–labeled CW cells, showing the intact ZO-1 junctions between two CW cells (cyan arrowheads) and between two CCW cells (magenta arrowheads) and intercellular gaps between CW and CCW cells (white arrowheads). The monolayer of cell mixture was labeled with Alexa Fluor 568 ZO-1 (1A12, red) and DAPI (blue); the CW cells were pretransfected with pmaxGFP (scale bar, 50 μm). (**L**) Percentage of positively stained ZO-1 of cell-cell junctions between two adjacent cells of the same or opposite chirality. Data are presented as average $\pm$ SD ($n = 12$ images and 72 junctions for each group). ***$P < 0.001$ by one-way ANOVAs with the Bonferroni-Holm method between groups. (**M**) Intercellular gap location at cell-cell junctions between two adjacent cells of the same or opposite chirality. Data are presented as average $\pm$ SD ($n = 12$ images for each group; $N = 82$ for the CW-CW group, $N = 126$ for the CW-CCW group, $N = 71$ for the CCW-CCW group). ***$P < 0.001$ by one-way ANOVAs with the Bonferroni-Holm method between groups.

kinase (FAK) by the inhibitor Y15 was not able to interfere with the Indo V–induced cell chirality switching to CCW (fig. S9). The well-known permeability agents, such as vascular endothelial growth factor (VEGF), platelet activating factor (PAF), and histamine, were not able to change endothelial cell chirality under either PKC activation or PKC inhibition condition (fig. S10). These data suggest that those known permeability regulation pathways are independent of the cell chirality mechanism revealed in this study.

PKCα isoform is required for the observed reversal of cell chirality

We first assayed PKC activation by detecting phosphorylated PKC and found that Indo V/TPA–treated cells exhibited a higher level of phosphorylated PKC/PKCα compared to controls (fig. S11, A and B). To confirm the effects of PKC activation on cell chirality, we cultured micropatterned hUVECs with a combination of Indo V/TPA and a broad PKC inhibitor, Ro-31-8425 (fig. S11, C and D), and found that the effects of Indo V/TPA on cell chirality reversal were suppressed.

We further investigated the specific isoform of PKC responsible for the reversal of intrinsic cell chirality. TPA and Indo V mimic the effects of DAG and therefore can activate DAG-dependent conventional and novel PKC isoforms. To differentiate between those two categories, we used a selective inhibitor of conventional PKC isoforms, Gö6976 (33). When treated with this drug, the cells were able to maintain their CW bias despite the presence of Indo V/TPA (fig. S11C). This indicates that a conventional PKC isoform is required for Indo V/TPA–induced reversal of cell chirality. On the basis of this result, we decided to focus on the effect of knockdown of PKCα, a conventional PKC isoform that is primarily expressed in endothelial cells (34, 35). To determine whether PKCα is required for Indo V/TPA–induced reversal of cell chirality, we generated stable cell lines with a short hairpin RNA (shRNA)–mediated knockdown system (Fig. 5, A to C, and fig. S12A). We found that knockdown of PKCα can rescue the reversal effects of either Indo V or TPA on cell chirality. The knockdown of the key PKC novel isoforms, PKCδ and PKCε, did not rescue the effects of Indo V/TPA treatment, but pan-PKC knockdown did (fig. S12, B and C). Overall, our results suggest that, with the PKC activators, the PKCα isoform is necessary for the reversal of intrinsic chiral bias of endothelial cells.

PI3K/AKT1/2 kinase activity is required for PKC-induced reversal of cell chirality

Next, we wanted to identify the downstream signaling pathways associated with activation of PKC-induced reversal of cell chirality. We focused on the PI3K/AKT kinase signaling pathway because it is a common effector of PKC signaling in regulating critical cellular behavior such as directional migration and this pathway is important for the establishment of LR asymmetry during development and implicated in congenital laterality disorders (36–39).

First, we determined whether PI3K signaling is required for PKC-related chirality reversal by using wortmannin, a selective inhibitor of PI3K (fig. S13). With concentrations of wortmannin (0.5 to 1 μM), the chirality of endothelial cells gradually regained a CW bias despite the presence of Indo V/TPA. These results show that PI3K signaling is required for PKC-induced switch of cell chirality.

Next, we analyzed the phosphorylation of AKT (pAKT) and found that Indo V/TPA–treated endothelial cells exhibited an overall elevated phosphorylation (fig. S14A). This result shows that AKT signaling was activated in the endothelial cells during the reversal of cell chirality.

Last, we investigated whether the AKT signaling pathway is required for PKC signaling–induced reversal of cell chirality. We used a combined treatment of AKT1/2 kinase inhibitor (AKT inhibitor VIII, a selective inhibitor of AKT signaling, 1 μM) and 30 nM Indo V or 0.5 nM TPA on micropatterned endothelial cells (fig. S14, B and C) and found that the AKT inhibitor rescued the effects of PKC activation and cells regained the CW bias. To confirm the role of the AKT1/2 kinase in PKC-regulated chirality reversal, we generated stable hUVEC lines expressing shRNA against AKT1/2 kinase (Fig. 5, D to F). The success of knockdown was confirmed by the quantitative real-time polymerase chain reaction (qPCR; fig. S15). The AKT1/2 knockdown cells did not respond to Indo V or TPA treatment on micropatterned rings and remained CW, as compared to the control knockdown group that switched to a CCW bias upon activation of PKC (Fig. 5, D to F). In summary, these data show that AKT1/2 kinase is required for the switch in endothelial cell chirality induced by small-molecule PKC activators.

DISCUSSION

Cell chirality was recently discovered and repeatedly demonstrated through various in vitro methods using microfabrication techniques (13, 14, 18, 40), but it has never been directly determined for a cellular monolayer without geometrical constraints or for planar or tubular biological tissues such as endothelium. In this study, we have demonstrated that individual cell chirality could be detected throughout cellular sheets through characterization of the LR-biased positioning of cell centroid to the nucleus-centrosome axis of the cell (Fig. 2D). The results are consistent with those from the 2D micropatterning-based approach. Compared to previously established methods, this new method defines an inherent LR chirality marker of individual cells, which does not rely on any physical boundaries such as those established through micropatterning. We have also successfully demonstrated that this new approach can be applied to analyze the endothelial cell chirality in biological tissues. Therefore, with genetic fluorescence labeling, this method has great potential to be used for live imaging for studying vascular diseases or LR asymmetry in embryonic development to advance the field of cell chirality. In the 2D monolayer model, the apicobasal axis of a cell is mostly perpendicular to the substrate, while the front-rear and LR axes are restrained in the 2D plane. Therefore, 2D analysis of the LR cell centroid positioning is sufficient to determine cell chirality for planar tissues. However, 3D imaging and reconstruction may be necessary to further improve the accuracy, especially for unflattened 3D vascular tissues.

We believe that cell chirality is responsible for endothelial permeability first increasing then decreasing with increased PKC activation for the following reasons. First, we did not find significant changes in cadherin types within the narrow range of drug doses used in this study for PKC activation. Second, the activation of PKCδ, a novel isoform that could potentially decrease endothelial permeability (41), is not likely to be responsible for the decreased permeability at 30 nM, since the K_i value of Indo V for binding with PKCδ is 8 nM, comparable to 6 nM for PKCα (42). Third, the interrupted cell junctions are preferentially localized between two cells with opposite chirality. This phenomenon cannot be possibly explained by the FAK or other chirality-independent pathways, which can be activated by PKC but do not alter cell chirality. Last, the loss of cell chirality and the highest permeability of the endothelial monolayer were found at the same
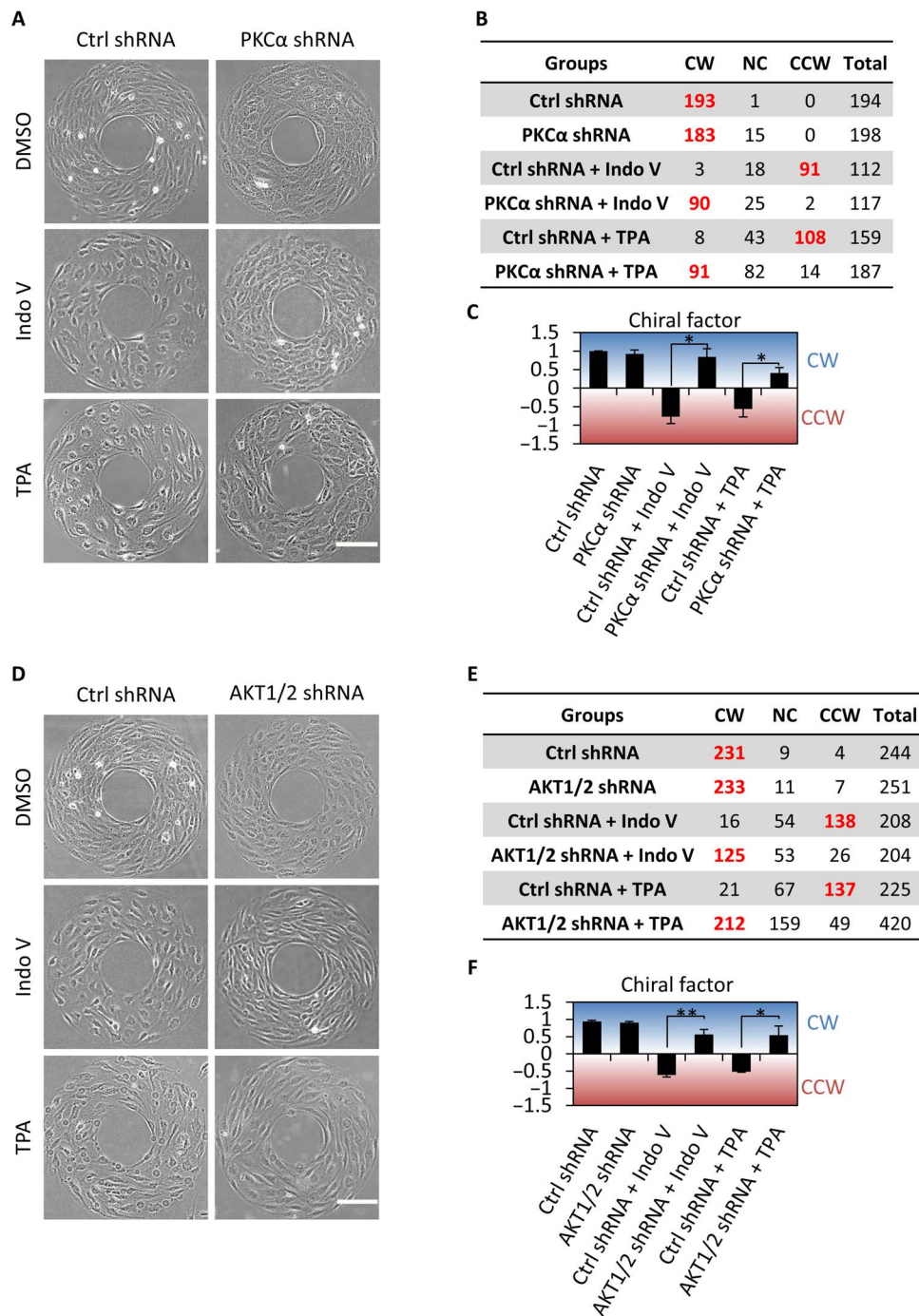
Fig. 5. PKC-mediated reversal of cell chirality from CW to CCW requires activation of PKCα and AKT1/2 kinase. (**A**) Phase-contrast images of the micropatterned hUVECs transfected with PKCα or control shRNA, untreated, or treated with 200 nM Indo V or 10 nM TPA (scale bar, 100 μm). (**B** and **C**) Numbers of CW, NC, and CCW rings and the corresponding CFs of hUVECs transfected with PKCα or control shRNA, untreated, or treated with 200 nM Indo V or 10 nM TPA. The bold red font in (B) indicates dominant chirality and a significant difference at $P < 0.05$ by the rank test. Data in (C) are presented as average ± SD; *$P < 0.05$ by Student's t test (unpaired, two tailed). (**D**) Phase-contrast images of the micropatterned hUVECs transfected with AKT1/2 or control shRNA, untreated, or treated with 200 nM Indo V or 10 nM TPA (scale bar, 100 μm). (**E** and **F**) Numbers of CW, NC, and CCW rings and the corresponding CFs of the hUVECs transfected with AKT1/2 or control shRNA, untreated, or treated with 200 nM Indo V or 10 nM TPA. The bold red font in (E) indicates dominant chirality and a significant difference at $P < 0.05$ by the rank test. Data in (F) are presented as average ± SD. *$P < 0.05$ and **$P < 0.01$ by Student's t test (unpaired, two tailed).

concentration of two different PKC activators (i.e., 20 nM Indo V and 0.2 nM TPA), suggesting that cell chirality is responsible for the increase of permeability.

The exact mechanism behind poor endothelial junction formation between cells of opposite chirality or no chirality is worthy of further investigation. One possible explanation is as follows. Endothelial cells have strong cell-cell adhesion and tend to exhibit emerging behaviors of cell clusters such as collective cell migration (43). As a result, the front-rear polarity of individual cells is likely to align in the same direction within a cluster. When the cells have opposite chirality, they will deviate from each other in the direction perpendicular to the front-rear axis, resulting in disrupted cellular junction formation. Because of the dynamic nature of cell morphology and organelle positioning, this hypothesis needs to be carefully evaluated in the future, possibly with live-cell imaging of fluorescently labeled organelles.

The reversal of endothelial cell chirality by PKC activation occurs possibly through the regulation of the actin network. The PKCα signaling has been demonstrated to alter the actin cytoskeleton network (44, 45) that regulates endothelial permeability (4, 44). Previously, it has also been shown that the level of α-actinin-1 cross-linking of F-actin radial fibers can regulate the directionality of intrinsic cytoskeletal swirling (18). Therefore, it is possible that low-level PKC activation can cause changes in the local cortical F-actin complex by altering the expression and functions of actin-coupling proteins such as MARCKS/GAP43, adducin, fascin, and ezrin/radixin/moesin proteins (45). Future research is necessary to elucidate whether and how these actin-related proteins are regulated by PKCα and their downstream effectors on cell chirality.

In this study, the implication of cell chirality in vascular physiological functions is demonstrated. The endothelial layer in different tissues of the vascular tree or under different physiological conditions may have different chiral properties, leading to varied cellular morphologies and endothelial permeability. For instance, the endothelial cells in tumor blood vessels have been found to be poorly organized when compared to those in normal tissue (46). Knowledge regarding chiral properties of endothelial cells in these situations is still largely limited and needs to be explored in the future.

In summary, endothelial permeability exhibits an initial increase and subsequent decrease of permeability at relatively low levels of PKC activation, associated with changes in intrinsic chirality of the cells by PKCα and PI3K/AKT signaling. The loss or randomization of cell chirality leads to the disrupted ZO-1 morphology between endothelial cells and the increased intercellular gap number and size, especially between those cells that do not have a clear chiral bias or have opposite chiral biases. Thus, our study reveals a new mechanism for the regulation of endothelial permeability through cell chirality. Our findings have broad implications in PKC-related vascular disorders and their treatments.

MATERIALS AND METHODS
Cell culture and transfection
The hUVECs (Lonza) were cultured in endothelial cell growth medium (EGM-Plus, Lonza) and used before passage 10. For fluorescence labeling, cells were transfected with the pmaxGFP vectors (Lonza), 24 hours before experiments, using the Amaxa 4D-Nucleofector system (Lonza). For gene knockdown, the cells were transfected with pan-PKC, PKCα, PKCδ, PKCε, AKT1/2 shRNA (Santa Cruz Biotechnology), or a negative control shRNA (Santa Cruz Biotechnology), which does

not lead to specific degradation of any cellular message. The stably transfected cells were established by further selection with antibiotics before use.

Permeability measurement
The permeability measurement was performed as described previously (47). For Transwell studies, endothelial cells were placed on fibronectin-coated Transwells (12-well, 0.4-μm pore; Thermo Fisher Scientific) at 600 cells/mm^2 and cultured with drugs, if needed, for 48 hours to reach confluency. The culture medium with 8 μM fluorescein isothiocyanate (FITC)–bovine serum albumin (BSA) (Sigma) was added to the upper chamber, while only culture medium was in the lower chamber. Every 30 min for the total duration of 120 min, 100 μl of sample solution was collected from the lower chamber followed by an immediate refill with fresh culture medium. The FITC-BSA concentration of collected samples was determined by the plate reader (Synergy H1, BioTek) with excitation/emission wavelengths of 490/525 nm. The permeability was calculated as

$$P_{albumin} = \frac{\Delta C / \Delta t}{C_0} \cdot \frac{V}{A} \qquad (1)$$

where $\Delta C / \Delta t$ is the rate of the FITC-BSA concentration increase in the lower chamber during the time interval Δt, C_0 is the FITC-BSA concentration in the upper chamber, assumed to be constant during the experiment, V is the medium volume in the lower chamber, and A is the area of the endothelial monolayer.

Transendothelial electrical resistance
The electrical resistance was measured using the Millicell ERS-2 Volt-Ohm Meter (Millipore) and calculated as

$$\text{TEER} = R_{total} - R_{filter} \qquad (2)$$

where R_{total} is the resistance of a cell monolayer plus filter and R_{filter} is the resistance of a control filter with no cells.

Cell patterning and chirality analysis
The cells were patterned as described in our previous study (14). Briefly, a master mold wafer was first fabricated with an SU-8 2050 photoresist (MicroChem) and chromium masks with ring-shaped (200 μm inner diameter and 500 μm outer diameter) features (CAD/Art Services). The polydimethylsiloxane (PDMS) stamp was then molded by incubating PDMS and curing solution mixture at a ratio of 10:1 on the wafer. The Ti-Au–coated glass slides were printed with 1-octadecanethiol (Sigma) using the PDMS stamp; subsequently, the slides were treated by the nonadhesive EG3 [HS-(CH$_2$)$_{11}$-EG3] (ProChimia) for at least 3 hours followed by a fibronectin (50 μg/ml, Sigma) coating for 30 min. Fifteen minutes after cell seeding, extra cells were washed off. The cells were then cultured with drugs, if needed, for 24 hours on micropatterns until confluency and fixed with 4% paraformaldehyde. High-resolution phase-contrast images were captured with a Zeiss AxioVision microscope (Carl Zeiss). A custom-written MATLAB (MathWorks) program was used to analyze the chirality by detecting the intensity gradient and circular statistics (14). Briefly, the cell alignment direction (blue lines in fig. S5, B and F) was calculated on the basis of the intensity gradient (32). Subsequently, the cell chirality of CW, NC, or CCW was determined using circular statistics based on

the distributions of cell alignment deviating from the circumferential directions (fig. S5, C and G) (48).

Drug treatment
For the cell monolayer cultured on the Transwell membrane for permeability, TEER, and immunostaining of junction proteins studies, 0 to 200 nM Indo V (Sigma) or 0 to 1 nM phorbol 12-myristate 13-acetate (TPA, Sigma) was added in both upper and lower chambers after cell attachment and maintained during the entire culture. Drugs were also present in the replenished media.

For cell mixture studies, the cells were pretreated with 200 nM Indo V for 24 hours before they were mixed with untreated cells at different ratios for experiments. The mixed cells were seeded at a density of 1200 cells/mm² on the fibronectin-coated Transwell and cultured 24 hours to reach confluency.

For cell chirality test on micropatterns, 30 nM Indo V or 0.5 nM TPA was used for PKC/PKCα activation; an AKT1/2 kinase inhibitor (AKT Inhibitor VIII trifluoroacetate salt hydrate, Sigma) and a PI3K inhibitor (wortmannin, Sigma) were used at 0 to 1 μM; Ro-31-8425 (Thermo Fisher Scientific) and Gö6976 (Santa Cruz Biotechnology) were used for PKC inhibition at 0 to 1 μM; and FAK inhibitor 14 (Y15, Sigma) was used at 0 to 10 μM. Among the known vascular permeability factors, recombinant human VEGF-165 (PeproTech), PAF (R&D Systems), or histamine dihydrochloride (R&D Systems) was used at 10 to 100 ng/ml, 0.1 to 1 μM, or 1 to 10 μM, respectively. Drug treatment was applied after 15 min of initial cell attachment on micropatterns until confluency and during the entire culture before fixation. For PKC and AKT phosphorylation Western blots, the cells were treated with 0.5 nM TPA or 30 nM Indo V after 15-min initial cell attachment and during the entire culture before fixation or lysis.

Immunofluorescence of in vitro cell culture
For junctional protein staining, the cells were cultured until confluency. The cells were then fixed with 4% paraformaldehyde (Santa Cruz Biotechnology), and the entire Transwell membrane was cut off for later steps. For micropatterning experiments, the cells were cultured on fibronectin-coated glass slides for 24 hours, followed by fixation with 4% paraformaldehyde. For cell membrane staining, the fixed cells were incubated with Alexa Fluor 488–conjugated WGA (5.0 μg/ml, Thermo Fisher Scientific) for 10 min. The cells were permeabilized with 0.2% Triton X-100/phosphate-buffered saline (PBS) for 15 min, blocked with 10% normal goat serum in 0.1% Triton X-100/PBS for 1 hour, and incubated with primary antibodies at 4°C overnight followed by 1-hour incubation of secondary antibodies at room temperature. Primary antibodies include mouse anti–ZO-1 (1A12, Thermo Fisher Scientific), mouse anti–VE-cadherin (F8, Santa Cruz Biotechnology), mouse anti–N-cadherin (H4, Santa Cruz Biotechnology), and rabbit anti-pericentrin (against both pericentrin-1 and pericentrin-2, Abcam). Secondary antibodies include Alexa Fluor 488/568 goat anti-mouse or anti-rabbit immunoglobulin G (IgG) H+L (Thermo Fisher Scientific). Last, samples were mounted in Fluoromount-G with or without DAPI (SouthernBiotech) and imaged using a fluorescence microscope (BZ-X700, Keyence) with an oil objective lens (60×/1.45, Nikon). The same imaging protocol was used for groups in the same experiment, including repeats and replicates.

Immunofluorescence of mouse vessels and human umbilical vein
Mice with mixed background without genetic deletion were maintained in accordance with protocols approved by the Institutional Animal Care and Use Committee in Albany Medical College. En face immuno-fluorescence staining of mouse vessels was described previously (49). Briefly, mice were euthanized with an intraperitoneal injection of sodium pentobarbital (0.1 mg/g of animal). A whole-body cardiac perfusion was performed by perfusing 0.9% sodium chloride saline followed by fixative (0.2% paraformaldehyde in PBS, pH 7.4) through the left ventricle of the heart after severing the right atrium. Thoracic aorta and vena cava were isolated and further fixed in 0.2% paraformaldehyde solution at 4°C for 1.5 hours. Fixed tissues were permeabilized in permeabilization buffer (PBS containing 0.2% Triton X-100) for 1 hour and subsequently incubated with blocking buffer [5.5% fetal bovine serum (FBS) in permeabilization buffer] for 1 hour at room temperature. Primary goat anti-VE-cadherin (C19, Santa Cruz Biotechnology), mouse anti-ZO-1 (1A12, Thermo Fisher Scientific), and rabbit anti-pericentrin (against both pericentrin-1 and pericentrin-2, Abcam) were diluted in staining buffer (2.75% FBS in permeabilization buffer) and incubated with tissue on a rocking platform for 16 hours at 4°C. Tissues were subsequently washed three times in permeabilization buffer at 30-min intervals. Secondary antibodies (Alexa Fluor 647–conjugated donkey anti-goat IgG H+L, Alexa Fluor 594–conjugated donkey anti-mouse IgG H+L, or Alexa Fluor 488–conjugated donkey anti-rabbit IgG H+L, Thermo Fisher Scientific) and DAPI diluted in staining buffer were added after the third wash and incubated at room temperature for 3 hours. Tissues were subsequently washed three times in permeabilization buffer and one time in PBS at 30 min per wash. After the PBS wash, vascular tissues were bisected along the direction of flow and mounted with a ProLong Diamond antifade mounting medium (Thermo Fisher Scientific).

Human umbilical cords from c-section procedures were obtained from the maternal-fetal medicine unit in Albany Medical Center in accordance with protocols approved by the Institutional Review Board. Human umbilical veins were carefully dissected away from the umbilical cords as described previously (50). The subsequent procedure for the en face immunofluorescence staining of the umbilical vein was the same as described for the mouse vessels. Z-stack images were obtained with 25× or 40× objectives using a Zeiss LSM 880 laser scanning confocal microscope with fast Airyscan module (Carl Zeiss).

Image analysis for junction protein and intercellular gaps
For the ZO-1 or VE-cadherin staining, the raw intensity profile of the entire cell junction and the average noise of multiple random regions were determined for each image and normalized by the average cell membrane intensity. The corrected intensity profile of junction protein was calculated as the ZO-1 or VE-cadherin intensity subtracted by the average intensity of cytoplasm. The reported staining percentage of ZO-1 or VE-cadherin was calculated as the percentage of pixels with positive intensity values. From the cell membrane staining, the gaps between cells were circled, counted, and measured by area using ImageJ. The results were presented as normalized numbers per square millimeter and percentage of the area. For the kurtosis of junction staining, the intensity profiles along a 5-μm line perpendicular to the VE-cadherin junction were used to determine the sharpness of the junction proteins at cell borders.

Image analysis for cell biases
For each fluorescence image of the endothelial cell layer stained for ZO-1/VE-cadherin, DAPI, and pericentrin-1, a manual segmentation (fig. S4B; red, cell borders) was first performed to separate individual cells following the cell junction staining. Positions of cell centroids (fig. S4B;

yellow, cell centroids) were then calculated using ImageJ. Similarly, the centroids of nuclei (fig. S4C; cyan, nuclear centroids) were calculated on the basis of the nuclear staining (fig. S4C; blue, nuclei). Then, cell borders (red), cell centroids (yellow), nuclear centroids (blue), and the centrosome channel (green) from the immunostaining were overlaid (fig. S4D). Last, the LR bias of each cell in the endothelial layer was determined according to the positional bias of the cell centroid (left side or right side) relative to the nucleus-centrosome (stained by anti-pericentrin) axis. A cell with a cell centroid overlapping the nucleus-centrosome axis was considered as nonbiased or neutral.

Time-lapse imaging
For cell motility study, cells were seeded at 600 cells/mm^2 in 48-well plates and treated with 0 to 30 nM Indo V for 24 hours, and the samples were mounted on the microscope (BZ-X700, Keyence) in a controlled working environment of 37°C and 5% CO_2. Time-lapse videos were captured with a phase-contrast objective lens (10×/0.3 objective, Nikon Instruments) every 5 min at a resolution of 1.31 μm per pixel for a total time of 4 hours. For each group, the movements of 20 single cells were tracked and analyzed with the MTrackJ plugin in ImageJ (1.50b, National Institutes of Health, USA).

For micropatterned cell migration analysis, cells were patterned on a gold-coated glass slide. After cells attached and spread, the slide was transferred face down onto a glass-bottom petri dish containing media in an environmental chamber (37°C and 5% CO_2) mounted within a Zeiss Axio Observer Z1 inverted microscope (Carl Zeiss). For time-lapse imaging, images were recorded every 5 min at a resolution of 1.56 μm per pixel (10×/0.3 objective, Carl Zeiss) for a total time of 48 to 65 hours. Cell tracking was performed for analyzing the directionality of cell migration along the ring boundaries using the MTrackJ plugin in ImageJ.

ELISA for PKC kinase activity
Cells were cultured with a PKC activator for 24 hours to reach confluency. Total protein of cell lysate was measured using a BCA protein assay kit (Thermo Fisher Scientific). Then, the PKC activities were quantitated following the instruction of the PKC kinase activity kit (Enzo Life Sciences) and normalized by total protein.

MTT assay
Cells were seeded at 600 cells/mm^2 in 96-well plates. The MTT assay was performed every 24 hours until 72 hours following the instructions of the MTT kit (Sigma). Absorbance at 570 and 690 nm was measured using a plate reader (Synergy H1, BioTek). Data were presented as absorbance at 570 nm subtracted by the background at 690 nm.

Quantitative real-time polymerase chain reaction
The gene knockdown was verified by qPCR. Briefly, total RNA was extracted from cells using the RNeasy Mini Kit (Qiagen) according to the manufacturer's protocol. Samples with equal amounts of total RNA were reversely transcribed into complementary DNA (cDNA), following the High-Capacity cDNA Reverse Transcription Kits (Applied Biosystems); the mRNA level of glyceraldehyde phosphate dehydrogenase (GAPDH), PKCα, PKCδ, PKCε, AKT1, or AKT2 was measured by the AB StepOne Real-Time PCR system (Applied Biosystems). Each reaction of a total 20-μl volume contained 10 μl of TaqMan Gene Expression Master Mix (2×, Applied Biosystems), 50 ng of cDNA templates, and 1 μl of TaqMan primers (20×, Applied Biosystems; GAPDH:

Hs02758991_g1; PKCα: Hs00925200_m1; PKCδ: Hs01090047_m1, PKCε: Hs00942886_m1, AKT1: Hs00178289_m1, AKT2: Hs01086099_m1). The ratio of target mRNA to GAPDH mRNA was calculated and normalized by the groups of knockdown using control shRNA.

Western blot
Cells were cultured in a T75 flask for 24 hours and then lysed on ice using lysis buffer (0.125 M tris at pH 6.8, 4% SDS, and 20% glycerol) with protease and phosphatase inhibitor cocktail (Sigma). Total protein was measured using a BCA protein assay kit (Thermo Fisher Scientific). Samples with equal amounts of total protein were subjected to 10% SDS–polyacrylamide gel electrophoresis and transferred to nitrocellulose membranes (Thermo Fisher Scientific). Then, the blots were blocked with 3% BSA in tris-buffered saline with Tween 20 and incubated with anti-pAKT (Ser^{473}, Cell Signaling Technologies), anti-pPKC (Thr^{497}, Abcam), anti-pPKCα (Thr^{638}, Thermo Fisher Scientific), or anti–β-actin (Abcam) followed by the horseradish peroxidase–conjugated secondary antibodies. The immunoreactive bands were developed using Pierce ECL Plus Substrate (Thermo Fisher Scientific) and imaged using ChemiDoc System (Bio-Rad).

Statistics
Data were presented as average ± SD unless indicated otherwise. One-way ANOVAs with the Bonferroni-Holm method for multiple comparisons were performed for the dose-dependent responses or multiple independent groups, using Daniel's XL Toolbox 7.2.6 in Microsoft Excel. Student's t test (unpaired, two tailed) was used for comparison between two groups. For the dominance of the number of CW and CCW rings, a rank test was used with MATLAB (MathWorks). The confidence level was set to 0.05 for all statistical tests.

SUPPLEMENTARY MATERIALS
Supplementary material for this article is available at http://advances.sciencemag.org/cgi/content/full/4/10/eaat2111/DC1

Detailed targeting sequences of shRNA plasmids
Fig. S1. The hUVEC monolayer permeability, TEER, ZO-1, intercellular gap number, and size with over 30 nM Indo V treatment.
Fig. S2. VE-cadherin morphology at different levels of PKC activation.
Fig. S3. PKC activity, metabolic activity, motility, and expression of cadherin proteins within the dosage range of Indo V causing cell chirality reversal.
Fig. S4. Chirality of endothelial cells in blood vessels.
Fig. S5. Determination of cell chirality using 2D micropatterning.
Fig. S6. Cell chirality of hUVECs as a function of Indo V concentration.
Fig. S7. Cell chirality and permeability of hUVECs as a function of TPA concentration.
Fig. S8. The CCW chirality persists for 48 hours after Indo V withdrawal.
Fig. S9. Cell chirality of hUVECs with FAK inhibition.
Fig. S10. PKC-mediated reversal of endothelial cell chirality persists with known vascular permeability factors.
Fig. S11. Activation of PKC signaling is required for the reversal of cell chirality.
Fig. S12. PKCα but not other isoforms is required for the PKC-mediated reversal of cell chirality.
Fig. S13. PI3K signaling is required for the PKC-mediated reversal of cell chirality.
Fig. S14. AKT1/2 kinase signaling is required for the PKC-mediated reversal of cell chirality.
Fig. S15. AKT1/2 kinase is down-regulated by shRNA.
Movie S1. The hUVEC migration on a micropatterned ring (inner diameter, 200 μm; outer diameter, 500 μm).
Movie S2. Cell migration on edges of the ring (inner diameter, 200 μm; outer diameter, 500 μm) during 42 to 46 hours in movie S1.
Movie S3. The hUVEC migration after TPA treatment on a micropatterned ring (inner diameter, 200 μm; outer diameter, 500 μm).
Movie S4. TPA-treated cell migration on edges of the ring (inner diameter, 200 μm; outer diameter, 500 μm) during 46 to 58 hours in movie S3.

REFERENCES AND NOTES

1. D. Mehta, A. B. Malik, Signaling mechanisms regulating endothelial permeability. *Physiol. Rev.* **86**, 279–367 (2006).

2. E. Dejana, Endothelial cell-cell junctions: Happy together. *Nat. Rev. Mol. Cell Biol.* **5**, 261–270 (2004).

3. E. Vandenbroucke, D. Mehta, R. Minshall, A. B. Malik, Regulation of endothelial junctional permeability. *Ann. N. Y. Acad. Sci.* **1123**, 134–145 (2008).

4. J. Gavard, J. S. Gutkind, VEGF controls endothelial-cell permeability by promoting the β-arrestin-dependent endocytosis of VE-cadherin. *Nat. Cell Biol.* **8**, 1223–1234 (2006).

5. W. L. Lee, A. S. Slutsky, Sepsis and endothelial permeability. *N. Engl. J. Med.* **363**, 689–691 (2010).

6. A. Hempel, C. Maasch, U. Heintze, C. Lindschau, R. Dietz, F. C. Luft, H. Haller, High glucose concentrations increase endothelial cell permeability via activation of protein kinase C alpha. *Circ. Res.* **81**, 363–371 (1997).

7. Y. Shen, V. Rattan, C. Sultana, V. K. Kalra, Cigarette smoke condensate-induced adhesion molecule expression and transendothelial migration of monocytes. *Am. J. Physiol.* **270**, H1624–H1633 (1996).

8. N. Kataoka, Y. Ogawa, K. Takeda, M. Sato, Relationship between permeability and endothelial cell morphology in rat aortae. *JSME Int. J. Series C* **42**, 811–817 (1999).

9. R. Ju, P. Cirone, S. Lin, H. Griesbach, D. C. Slusarski, C. M. Crews, Activation of the planar cell polarity formin DAAM1 leads to inhibition of endothelial cell proliferation, migration, and angiogenesis. *Proc. Natl. Acad. Sci. U.S.A.* **107**, 6906–6911 (2010).

10. L. Q. Wan, K. Ronaldson, M. Guirguis, G. Vunjak-Novakovic, Micropatterning of cells reveals chiral morphogenesis. *Stem Cell Res. Ther.* **4**, 24 (2013).

11. L. Q. Wan, G. Vunjak-Novakovic, Micropatterning chiral morphogenesis. *Commun. Integr. Biol.* **4**, 745–748 (2011).

12. L. Q. Wan, A. S. Chin, K. E. Worley, P. Ray, Cell chirality: Emergence of asymmetry from cell culture. *Philos. Trans. R. Soc. Lond. B Biol. Sci.* **371**, 20150413 (2016).

13. T. H. Chen, J. J. Hsu, X. Zhao, C. Guo, M. N. Wong, Y. Huang, Z. Li, A. Garfinkel, C. M. Ho, Y. Tintut, L. L. Demer, Left-right symmetry breaking in tissue morphogenesis via cytoskeletal mechanics. *Circ. Res.* **110**, 551–559 (2012).

14. L. Q. Wan, K. Ronaldson, M. Park, G. Taylor, Y. Zhang, J. M. Gimble, G. Vunjak-Novakovic, Micropatterned mammalian cells exhibit phenotype-specific left-right asymmetry. *Proc. Natl. Acad. Sci. U.S.A.* **108**, 12295–12300 (2011).

15. J. Xu, A. Van Keymeulen, N. M. Wakida, P. Carlton, M. W. Berns, H. R. Bourne, Polarity reveals intrinsic cell chirality. *Proc. Natl. Acad. Sci. U.S.A.* **104**, 9296–9300 (2007).

16. K. E. Worley, D. Shieh, L. Q. Wan, Inhibition of cell-cell adhesion impairs directional epithelial migration on micropatterned surfaces. *Integr. Biol.* **7**, 580–590 (2015).

17. K. Taniguchi, R. Maeda, T. Ando, T. Okumura, N. Nakazawa, R. Hatori, M. Nakamura, S. Hozumi, H. Fujiwara, K. Matsuno, Chirality in planar cell shape contributes to left-right asymmetric epithelial morphogenesis. *Science* **333**, 339–341 (2011).

18. Y. H. Tee, T. Shemesh, V. Thiagarajan, R. F. Hariadi, K. L. Anderson, C. Page, N. Volkmann, D. Hanein, S. Sivaramakrishnan, M. M. Kozlov, A. D. Bershadsky, Cellular chirality arising from the self-organization of the actin cytoskeleton. *Nat. Cell Biol.* **17**, 445–457 (2015).

19. W. Liu, Y. Bao, M. L. Lam, T. Xu, K. Xie, H. S. Man, E. Y. Chan, N. Zhu, R. H. Lam, T. H. Chen, Nanowire magnetoscope reveals a cellular torque with left-right bias. *ACS Nano* **10**, 7409–7417 (2016).

20. A. Davison, G. S. McDowell, J. M. Holden, H. F. Johnson, G. D. Koutsovoulos, M. M. Liu, P. Hulpiau, F. Van Roy, C. M. Wade, R. Banerjee, F. Yang, S. Chiba, J. W. Davey, D. J. Jackson, M. Levin, M. L. Blaxter, Formin is associated with left-right asymmetry in the pond snail and the frog. *Curr. Biol.* **26**, 654–660 (2016).

21. K. Sato, T. Hiraiwa, E. Maekawa, A. Isomura, T. Shibata, E. Kuranaga, Left-right asymmetric cell intercalation drives directional collective cell movement in epithelial morphogenesis. *Nat. Commun.* **6**, 10074 (2015).

22. P. Geraldes, G. L. King, Activation of protein kinase C isoforms and its impact on diabetic complications. *Circ. Res.* **106**, 1319–1331 (2010).

23. D. Geiges, T. Meyer, B. Marte, M. Vanek, G. Weissgerber, S. Stabel, J. Pfeilschifter, D. Fabbro, A. Huwiler, Activation of protein kinase C subtypes alpha, gamma, delta, epsilon, zeta, and eta by tumor-promoting and nontumor-promoting agents. *Biochem. Pharmacol.* **53**, 865–875 (1997).

24. J. A. Gruenhagen, E. S. Yeung, Investigation of G protein-initiated, Ca²⁺-dependent release of ATP from endothelial cells. *Biochim. Biophys. Acta* **1693**, 135–146 (2004).

25. I. Fleming, J. Bauersachs, A. Schäfer, D. Scholz, J. Aldershvile, R. Busse, Isometric contraction induces the Ca²⁺-independent activation of the endothelial nitric oxide synthase. *Proc. Natl. Acad. Sci. U.S.A.* **96**, 1123–1128 (1999).

26. O. Tornavaca, M. Chia, N. Dufton, L. O. Almagro, D. E. Conway, A. M. Randi, M. A. Schwartz, K. Matter, M. S. Balda, ZO-1 controls endothelial adherens junctions, cell-cell tension, angiogenesis, and barrier formation. *J. Cell Biol.* **208**, 821–838 (2015).

27. B. Schulz, J. Pruessmeyer, T. Maretzky, A. Ludwig, C. P. Blobel, P. Saftig, K. Reiss, ADAM10 regulates endothelial permeability and T-Cell transmigration by proteolysis of vascular endothelial cadherin. *Circ. Res.* **102**, 1192–1201 (2008).

28. A. J. Ridley, M. A. Schwartz, K. Burridge, R. A. Firtel, M. H. Ginsberg, G. Borisy, J. T. Parsons, A. R. Horwitz, Cell migration: Integrating signals from front to back. *Science* **302**, 1704–1709 (2003).

29. M. Théry, V. Racine, M. Piel, A. Pépin, A. Dimitrov, Y. Chen, J. B. Sibarita, M. Bornens, Anisotropy of cell adhesive microenvironment governs cell internal organization and orientation of polarity. *Proc. Natl. Acad. Sci. U.S.A.* **103**, 19771–19776 (2006).

30. R. J. Petrie, A. D. Doyle, K. M. Yamada, Random versus directionally persistent cell migration. *Nat. Rev. Mol. Cell Biol.* **10**, 538–549 (2009).

31. J. Suo, D. E. Ferrara, D. Sorescu, R. E. Guldberg, W. R. Taylor, D. P. Giddens, Hemodynamic shear stresses in mouse aortas: Implications for atherogenesis. *Arterioscler. Thromb. Vasc. Biol.* **27**, 346–351 (2007).

32. W. J. Karlon, P. P. Hsu, S. Li, S. Chien, A. D. McCulloch, J. H. Omens, Measurement of orientation and distribution of cellular alignment and cytoskeletal organization. *Ann. Biomed. Eng.* **27**, 712–720 (1999).

33. G. Martiny-Baron, M. G. Kazanietz, H. Mischak, P. M. Blumberg, G. Kochs, H. Hug, D. Marmé, C. Schächtele, Selective inhibition of protein kinase C isozymes by the indolocarbazole Gö 6976. *J. Biol. Chem.* **268**, 9194–9197 (1993).

34. H. Li, S. A. Oehrlein, T. Wallerath, I. Ihrig-Biedert, P. Wohlfart, T. Ulshöfer, T. Jessen, T. Herget, U. Forstermann, H. Kleinert, Activation of protein kinase C α and/or ε enhances transcription of the human endothelial nitric oxide synthase gene. *Mol. Pharmacol.* **53**, 630–637 (1998).

35. H. Xu, P. Czerwinski, M. Hortmann, H. Y. Sohn, U. Förstermann, H. Li, Protein kinase C α promotes angiogenic activity of human endothelial cells via induction of vascular endothelial growth factor. *Cardiovasc. Res.* **78**, 349–355 (2008).

36. T. Casar Tena, M. D. Burkhalter, M. Philipp, Left-right asymmetry in the light of TOR: An update on what we know so far. *Biol. Cell* **107**, 306–318 (2015).

37. M. Minhajuddin, K. M. Bijli, F. Fazal, A. Sassano, K. I. Nakayama, N. Hay, L. C. Platanias, A. Rahman, Protein kinase C-δ and phosphatidylinositol 3-kinase/Akt activate mammalian target of rapamycin to modulate NF-κB activation and intercellular adhesion molecule-1 (ICAM-1) expression in endothelial cells. *J. Biol. Chem.* **284**, 4052–4061 (2009).

38. G. Xue, B. A. Hemmings, PKB/Akt-dependent regulation of cell motility. *J. Natl. Cancer Inst.* **105**, 393–404 (2013).

39. B. P. Ziemba, J. E. Burke, G. Masson, R. L. Williams, J. J. Falke, Regulation of PI3K by PKC and MARCKS: Single-molecule analysis of a reconstituted signaling pathway. *Biophys. J.* **110**, 1811–1825 (2016).

40. M. J. Raymond Jr., P. Ray, G. Kaur, A. V. Singh, L. Q. Wan, Cellular and nuclear alignment analysis for determining epithelial cell chirality. *Ann. Biomed. Eng.* **44**, 1475–1486 (2016).

41. E. O. Harrington, J. L. Brunelle, C. J. Shannon, E. S. Kim, K. Mennella, S. Rounds, Role of protein kinase C isoforms in rat epididymal microvascular endothelial barrier function. *Am. J. Respir. Cell Mol. Biol.* **28**, 626–636 (2003).

42. M. G. Kazanietz, L. B. Areces, A. Bahador, H. Mischak, J. Goodnight, J. F. Mushinski, P. M. Blumberg, Characterization of ligand and substrate specificity for the calcium-dependent and calcium-independent protein kinase C isozymes. *Mol. Pharmacol.* **44**, 298–307 (1993).

43. U. R. Michaelis, Mechanisms of endothelial cell migration. *Cell. Mol. Life Sci.* **71**, 4131–4148 (2014).

44. R. Sandoval, A. B. Malik, R. D. Minshall, P. Kouklis, C. A. Ellis, C. Tiruppathi, Ca²⁺ signaling and PKCα activate increased endothelial permeability by disassembly of VE-cadherin junctions. *J. Physiol.* **533**, 433–445 (2001).

45. C. Larsson, Protein kinase C and the regulation of the actin cytoskeleton. *Cell. Signal.* **18**, 276–284 (2006).

46. H. Hashizume, P. Baluk, S. Morikawa, J. W. McLean, G. Thurston, S. Roberge, R. K. Jain, D. M. McDonald, Openings between defective endothelial cells explain tumor vessel leakiness. *Am. J. Pathol.* **156**, 1363–1380 (2000).

47. J. Fan, B. Cai, M. Zeng, Y. Hao, F. G. Giancotti, B. M. Fu, Integrin β4 signaling promotes mammary tumor cell adhesion to brain microvascular endothelium by inducing ErbB2-mediated secretion of VEGF. *Ann. Biomed. Eng.* **39**, 2223–2241 (2011).

48. N. I. Fisher, *Statistical Analysis of Circular Data* (Cambridge Univ. Press, 1993).

49. Y. W. Lu, A. M. Lowery, L.-Y. Sun, H. A. Singer, G. Dai, A. P. Adam, P. A. Vincent, J. J. Schwarz, Endothelial myocyte enhancer factor 2c inhibits migration of smooth muscle cells through fenestrations in the internal elastic lamina. *Arterioscler. Thromb. Vasc. Biol.* **37**, 1380–1390 (2017).

50. D. van Geemen, M. W. J. Smeets, A.-M. D. van Stalborch, L. A. E. Woerdeman, M. J. A. P. Daemen, P. L. Hordijk, S. Huveneers, F-actin–anchored focal adhesions distinguish endothelial phenotypes of human arteries and veins. *Arterioscler. Thromb. Vasc. Biol.* **34**, 2059–2067 (2014).

Citation: J. Fan, P. Ray, Y. Lu, G. Kaur, J. J. Schwarz, L. Q. Wan, Cell chirality regulates intercellular junctions and endothelial permeability. *Sci. Adv.* **4**, eaat2111 (2018).